QCL-based mid-infrared hyperspectral imaging of multilayer polymer oxygen barrier-films

Robert Zimmerleiter, R. Nikzad-Langerodi, Cyril Ruckebusch, Matthias Godejohann, J. Kilgus, K. Duswald, M. Brandstetter

Polymer Testing 98 (2021) 107190

Contents lists available at ScienceDirect

Polymer Testing

journal homepage: http://www.elsevier.com/locate/polytest

QCL-based mid-infrared hyperspectral imaging of multilayer polymer oxygen barrier-films

Robert Zimmerleiter [a,*], Ramin Nikzad-Langerodi [b], Cyril Ruckebusch [c], Matthias Godejohann [d], Jakob Kilgus [a], Kristina Duswald [a], Markus Brandstetter [a]

[a] RECENDT – Research Center for Non-Destructive Testing GmbH, Altenberger Straße 69, 4040, Linz, Austria
[b] SCCH – Software Competence Center Hagenberg, Softwarepark 21, 4232, Hagenberg, Austria
[c] LASIRE - Laboratory for Advanced Spectroscopy, Interactions, Reactivity and Environment, U LILLE, CNRS, 4 Rue Paul Duez, F 59000, Lille, France
[d] MG Optical Solutions GmbH, Industriestraße 23, 86919, Utting am Ammersee, Germany

ARTICLE INFO

Keywords:
Quantum cascade laser
Mid-infrared spectroscopy
Hyperspectral imaging
Multi-layer polymer film
Principal component analysis
Multivariate curve resolution

ABSTRACT

In this work, mid-infrared hyperspectral images of multilayer polymer film (MLPF) cross sections are acquired with a high-speed quantum cascade laser (QCL) based mid-infrared microscope and analyzed using different data analysis techniques. The investigated MLPF is a polypropylene (PP) and ethylene-vinyl alcohol co-polymer (EVOH) composite commonly used for food packaging due to its outstanding barrier characteristics. Pure band integration of supposedly selective absorption bands for the two constituents of the MLPF is compared to principal component analysis (PCA) and multivariate curve resolution (MCR) algorithms regarding the ability to spatially resolve the differently composed areas in the MLPF. While both pure band integration and PCA are strongly affected by common physical artifacts in the spectral data, such as sample tilt, scattering or interference effects, MCR managed to give a clear picture of the composition of the MLPF, which matches the actual situation given by the manufacturing process. The obtained results can guide the way to the application of high-performance mid-infrared spectroscopic instrumentation for spatially resolved polymer analysis by meaningful interpretation of hyperspectral image data.

1. Introduction

Over the past decades, hyperspectral imaging (HSI) has been widely adopted in areas like e.g. food quality and safety assessment [1], precision agriculture [2], forensics [3,4], safety and homeland security [5] or medical diagnostics [6,7]. Mid-infrared (MIR) radiation has been particularly useful in the context of extracting spatially resolved chemical information as it features high chemical sensitivity and specificity due to the excitation of characteristic fundamental molecular vibrations, while at the same time allowing for a decent spatial resolution in the micrometer range. The recent advent of high-power MIR light sources, such as supercontinuum lasers (SCLs) [8,9] and quantum cascade lasers (QCLs) [10–12] has not only led to a dramatic increase in the sensitivity of MIR spectroscopy, but has also opened up the possibility for micro-spectroscopy with a spatial resolution down to the diffraction-limit [13–15].

In the current contribution the analysis of multi-layer polymer films (MLPFs) consisting of polypropylene (PP) end ethylene-vinyl alcohol co-polymer (EVOH) by means of QCL-based MIR microscopy is demonstrated. Such MLPFs are widely used e.g. in the food industry as packaging materials that convey physical protection to dietary products, increase their shelf-life and support preservation of aroma, flavor and color [16]. In particular, widely used EVOH-PP composites have outstanding barrier characteristics with regard to gases, water, odors and fats and are well recyclable [17]. In order to achieve these advantageous effects, the thickness of the EVOH barrier layer should not be too thin. In contrast, however, due to the significantly higher cost of EVOH compared to PP, it is beneficial to limit the quantity of EVOH in the packaging material. Thus, the production process of MLPFs needs to be optimized to achieve a controlled thickness within certain boundaries, depending on the exact application of the film, to ensure simultaneous functionality and cost-efficiency. In order to achieve the necessary spatially resolved chemical information, HSI provides a very practical tool for at-line analysis of the EVOH layer thickness and the structure of the EVOH-PP interface in cross sections of such films.

* Corresponding author.
E-mail address: robert.zimmerleiter@recendt.at (R. Zimmerleiter).

https://doi.org/10.1016/j.polymertesting.2021.107190
Received 11 March 2021; Received in revised form 29 March 2021; Accepted 5 April 2021
Available online 22 April 2021

2. Experimental

2.1. Sample preparation

The investigated multi-layer polymer films consisted of a thin EVOH layer sandwiched between two much thicker PP layers. Since these polymer films are produced by applying high pressure to the powdered polymers, a mixing layer between the PP and EVOH layers is expected to form. For analysis of the layered structure of these polymer films, samples were carefully cut by hand using a microtome blade to obtain a cross sectional piece of approximately 200 μm – 300 μm thickness, as shown in Fig. 1 (a) and subsequently fixed to a microscope slide using adhesive tape. From previous measurements using a conventional MIR Fourier-transform (FTIR) microscope with a thermal emitter (LUMOS, Bruker, Germany), it was known that the EVOH thickness in these multi-layer films is typically in the range of approximately 30 μm – 160 μm.

2.2. MIR imaging

MIR hyperspectral images were recorded using a state-of-the-art QCL-based MIR microscope (Spero®QT, Daylight Solutions, USA) in reflection mode. A schematic drawing of the optical setup is shown in Fig. 1 (b). Inside the microscope, four external-cavity QCLs (EC-QCLs) scan over a very broad wavelength range covering 1800 cm^{-1} to 950 cm^{-1} or parts of it, if preferred, to increase acquisition speed. The uncooled microbolometer FPA camera (μ-bolometer) of the microscope measures 480 × 480 pixels simultaneously. The acquisition of one hyperspectral data cube (230,400 spectra) with a spectral resolution of 2 cm^{-1} over the whole available spectral range takes less than 45 s per image with diffraction limited spatial resolution. The hyperspectral images presented herein were recorded using a 12.5× high magnification objective (NA 0.7), resulting in a field of view (FOV) of 650 × 650 μm^2. Due to this high FOV, large areas can be measured with a single shot resulting in unprecedented measurement speed, even when compared to modern FTIR-MIR microscopes using FPA detectors. This is enabled by the high brilliance of the employed laser sources, in contrast to the low brilliance thermal emitters used in FTIR-MIR microscopes. Furthermore, thermal emitters do not allow for diffraction limited resolution, which is another consequence of their low brilliance. Moreover, the high output power of QCLs makes liquid nitrogen cooling of the camera obsolete which allows for seamless 24/7-operation capability without cost for consumables. This is highly advantageous especially for industrial applications and automated routine measurements.

Two different areas (later referred to as area 1 and area 2) were measured on the same sample with the QCL-based MIR microscope. During data analysis, we discovered that the sample on the microscope slide was not perfectly aligned to the focal plane and the leftmost 100 pixels (approximately 135 μm) were cut from the image of area 2 since these pixels were clearly out of focus.

2.3. Data analysis

2.3.1. Spectral preprocessing

The 480 × 480 × 424 and 380 × 480 × 424 three-way hyperspectral cubes obtained with the QCL microscope from area 1 and 2 were unfolded in the spatial direction yielding two-way arrays of dimensions 230,400 × 424 and 182,400 × 424 (i.e. pixels times spectral channels), respectively. Due to the lack of EVOH-specific absorption bands in the spectral range 1800 cm^{-1} – 1550 cm^{-1}, only the range 1550 cm^{-1} – 950 cm^{-1} was considered resulting in reduced two-way arrays of size 230,400 × 300 and 182,400 × 300. Baseline correction was performed using the asymmetric least squares smoothing algorithm described in Ref. [18] with the following parameter setting: $\lambda = 10^5$, $p = 0.01$ and 10 iterations per spectrum. In the case of PCA-analysis, mean centering was additionally applied to the spectral data.

2.3.2. Principal component analysis (PCA)

Principal component analysis (PCA) is a common starting point for the analysis of spectral datasets. PCA finds a (usually small) set of so-called principal components (PCs) that summarize a large portion of the variation in data [19].
Formally, PCA solves

$$\min_{\mathbf{T},\mathbf{P}} \left|\left|\mathbf{X} - \mathbf{T}\mathbf{P}^T\right|\right|_F^2 \text{ such that } \mathbf{P}^T\mathbf{P} = \mathbf{I} \text{ and } \mathbf{T}^T\mathbf{T} = \mathbf{D} \quad (1)$$

where $\mathbf{X}$, $\mathbf{T}$ and $\mathbf{P}$ denote the $N \times K$ (samples times variables) matrix holding the spectra, the $N \times A$ scores and $K \times A$ loadings matrix, respectively. The matrix $\mathbf{D}$ in Eq. (1) is a diagonal matrix of dimensions $N \times N$ whose elements are proportional to the explained variance of each PC and $\mathbf{I}$ is the identity matrix of appropriate size. For spectral datasets, a small number of PCs (i.e. $A \ll K$) is usually sufficient to describe the meaningful spectral variation in $\mathbf{X}$, which can be attributed

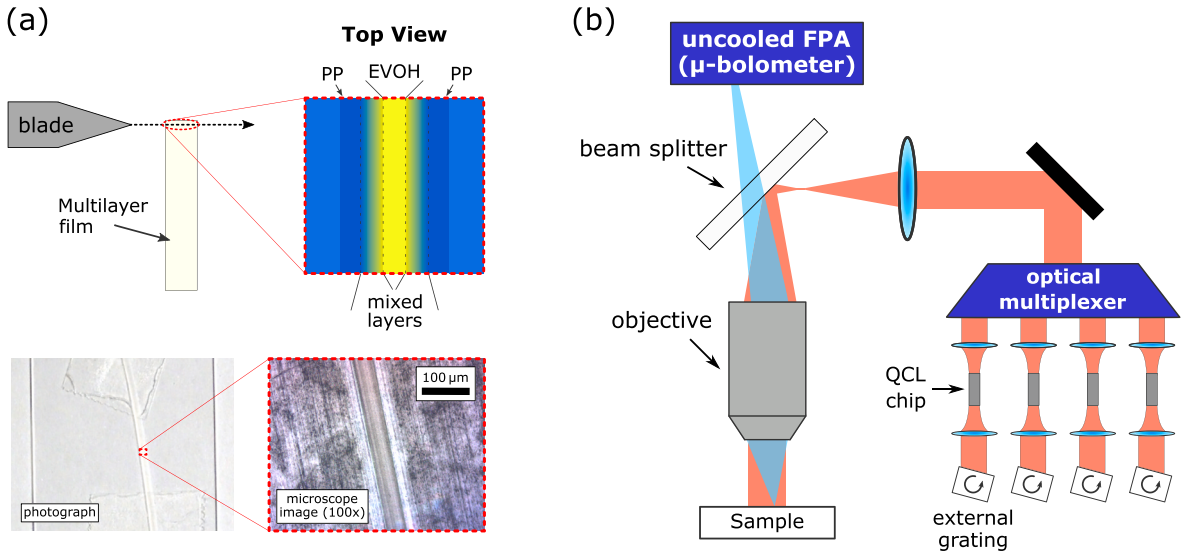

Fig. 1. (a) Top – Schematic drawing of the sample preparation process, with schematic top view of the prepared sample where the individual layers in the film are indicated. Bottom – Photograph and microscope image of a multi-layer polymer film sample. (b) Simplified drawing of the optical setup in the QCL-microscope in reflection mode.

to the high redundancy that is naturally encoded in the spectral variables (i.e. collinearity).

The number of chemically or physically distinct sources of spectral variation (i.e. the rank A of the decomposition) is not known in most practical situations, due to lacking or incomplete knowledge about the chemical composition of the sample and limited understanding of the physical phenomena affecting the measurement (e.g. background effects like baselines, scattering or interference effects). In such cases, A can be estimated from the PCA analysis. For an in-depth discussion on application of PCA to spectral data we refer to Ref. [20]. In any case, PCA provides a reasonable starting point for the exploration and decomposition of hyperspectral data sets.

The second advantage of PCA is rooted in the orthogonality constraints imposed on the scores and loadings, which are necessary for the model to be unique. As a result, each PC describes a different source of variation in the data that can be analyzed separately. By convention, the first PC describes most of the variation in **X**, the second PC most of the variation not explained by the first one and so on. In order to visualize most of the spectral information contained in the hyperspectral data cubes, we visualized the scores of each pixel on the first 3 PCs using false color images (see Fig. 4). PCA analysis was performed using in-house code written in Python 3.6.

2.3.3. Multivariate curve resolution (MCR)

Multivariate curve resolution (MCR) aims at a low-rank bilinear decomposition of the (hyperspectral) data, thus providing a simple and easily interpretable representation of the data via chemically meaningful factors. In contrast to PCA, where the scores and loadings matrices **T** and **P** correspond to abstract factors resulting from a purely mathematical decomposition, MCR can provide concentration distribution profiles **C** and spectra **S** of the pure components that compose the observed spectral mixture (i.e. the acquired spectral data) [21]. MCR solves

$$\min_{\mathbf{C},\mathbf{S}} \left|\left| \widehat{\mathbf{X}}^{(A)} - \mathbf{C}\mathbf{S}^T \right|\right|_F^2, \tag{2}$$

where

$$\widehat{\mathbf{X}}^{(A)} = \sum_{i=1}^{A} \mathbf{t}_i \mathbf{p}_i^T \tag{3}$$

is the rank-A approximation of **X** (i.e. the sum of the first A PCs). The solution is found by alternatingly solving for **C**, while keeping **S** constant and vice versa until convergence, i.e.

$$\widehat{\mathbf{C}} = \widehat{\mathbf{X}}\mathbf{S}^{\dagger} \text{ and } \widehat{\mathbf{S}} = \left(\mathbf{C}^{\dagger}\widehat{\mathbf{X}}\right)^T \tag{4}$$

with $\mathbf{C}^{\dagger} = (\mathbf{C}^T\mathbf{C})^{-1}\mathbf{C}^T\widehat{\mathbf{X}}$ and $\mathbf{S}^{\dagger} = (\mathbf{S}^T\mathbf{S})^{-1}\mathbf{S}^T\widehat{\mathbf{X}}$ (i.e. the pseudo inverses of **C** and **S**). This procedure is commonly known as alternating least squares (ALS). Additionally, constraints can be added to the concentration and/or spectral profiles of the components (e.g. non-negativity or unimodality). We used multivariate curve resolution alternating least squares (MCR-ALS) [22], which is an algorithm that iteratively solves concentration and spectral profiles with constraints. One important point regarding the application of constraints is that they can be optionally applied to all or some of the compounds in the analyzed system on the concentration and/or spectral direction. In addition, image processing constraints [23] can be applied on the concentration distribution maps obtained with HSI data. Most of the progress and generalized use of MCR relates to the application of constraints and the possibility to work with multiset matrices. In particular, these aspects allow to dramatically reduce ambiguities that are inherent to any factor analysis decomposition method (i.e. the phenomenon that different combinations of $\widehat{\mathbf{C}}$ and $\widehat{\mathbf{S}}$ fit the data equally well) [24].

As already mentioned, MCR-ALS can analyze single data matrices, but advantage can also be taken from the simultaneous analysis of multiset data structures formed by several concatenated data matrices [25]. The multiset data was constructed by merging the data corresponding to area 1 and area 2 resulting in a 412,800 × 300 (i.e. pixels times spectral channels). This data augmentation scheme implies that spectral information is (partially) shared between the two data sets. MCR-ALS was jointly applied to this multiset data under a non-negativity constraint on both spectral profiles and concentration maps, i.e. forcing the entries of $\widehat{\mathbf{S}}$ and $\widehat{\mathbf{C}}$ to be non-negative. Furthermore, a constraint was applied to encode the absence of a component in one of the two images (i.e. in area 1 or area 2, respectively).

MCR-ALS requires initial estimates of $\widehat{\mathbf{S}}$ to be provided. To this end, we applied the procedure for pixel selection described in Ref. [26] that allows for better estimation of the number of components that should be incorporated in the MCR decomposition model. One striking feature of MCR-ALS is multiset data analysis, which aims here at helping the separation of highly overlapping profiles in the spectral regime.

To assess the quality of the decomposition, the lack of fit (LOF), defined in Eq. (5) is the most common figure of merit in MCR to evaluate the difference between raw and reproduced data [22].

$$\mathrm{LOF}(\%) = 100 \cdot \sqrt{\frac{\sum \left(x_{ij} - \widehat{x}_{ij}\right)^2}{\sum x_{ij}^2}} = 100 \cdot \sqrt{\frac{\sum e_{ij}^2}{\sum x_{ij}^2}} \tag{5}$$

where x_{ij} is one element of the data matrix **X** and $\widehat{x}_{ij}$ is the analogous element of the matrix $\widehat{\mathbf{X}}^{(A)}$ reproduced using MCR-ALS as given in Eq. (3). Additionally, the percentage of explained variance r^2 as defined in Eq. (6) is usually reported to indicate the fit quality:

$$r^2(\%) = 100 \cdot \sqrt{\frac{\sum x_{ij}^2 - \sum e_{ij}^2}{\sum x_{ij}^2}} \tag{6}$$

All the calculations were performed in Matlab 7.5 (The MathWorks Ltd., Massachusetts). The used MCR routines are freely available on the web at http://www.mcrals.info/.

3. Results and discussion

Two areas of the MLPF-sample were investigated using QCL-based MIR hyperspectral imaging. Area 1 covers the whole FOV of the utilized microscope (650 × 650 μm^2), while for area 2 the leftmost 135 μm were removed because they were out of focus and thus do not contribute any valid chemical information. The integrated value of the absorbance in the spectral range 1550 cm^{-1} – 950 cm^{-1} for both areas is depicted as a grey-scale image on the top in Fig. 2. On the bottom, individual as well as the average absorbance spectrum with standard deviations is shown to visualize the rather broad variation in the obtained spectra, mainly due to scattering effects originating from the non-planar sample surface. Further studies using an objective with lower NA and samples with different roughness should be performed in the near future to investigate the main reasons for the observed variation in the spectra. Nevertheless, characteristic absorption bands for PP can be clearly identified in the average spectrum (see also Fig. 3).

Fig. 3 (bottom) shows reference spectra of PP and EVOH in blue and orange, respectively, collected on pure materials with a conventional FTIR microscope (LUMOS, Bruker, Germany) in reflection geometry. On the top in the same figure, the integrated absorbance of the characteristic PP band at 1168 cm^{-1} and the intramolecular hydrogen bond affected ν(C–O) stretching band of EVOH [27] at around 1080 cm^{-1} are depicted as false color images for both areas, where low values are shown in blue and high values in red. Under ideal conditions (i.e. in the absence of physical effects such as scattering), the latter would be selective for the secondary alcohol in EVOH and the former for backbone ν(C–C) stretching, $\rho(CH_3)$ rocking and δ(C–H) deformation vibrations

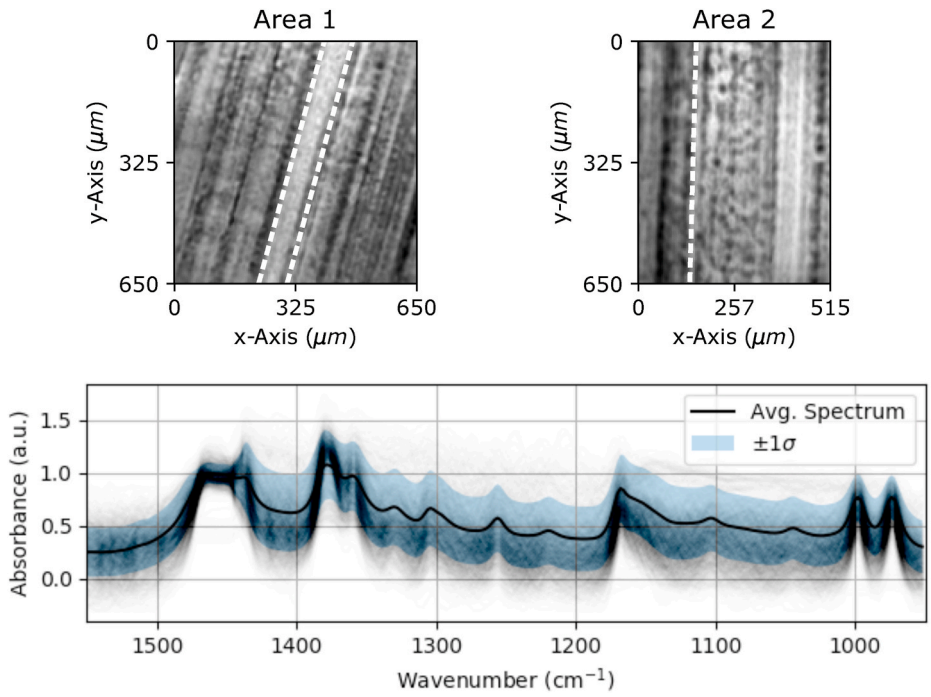

Fig. 2. Acquired data for the two investigated areas on the MLPF sample (area 1 and area 2). Top panel: Integrated absorption spectrum in the spectral range 1550 cm^{-1} – 950 cm^{-1} for the two investigated areas. White dashed lines indicate the borders between EVOH-rich and PP-rich areas as determined by MCR (see Fig. 5). Bottom: Individual (grey) and average (black) absorbance spectra for both areas with standard deviations.

[28] associated with stereoregularity/tacticity of PP polymers [29]. The intensity distribution of the ν(C–O) band in area 1 (Fig. 3, top left) clearly suggests that the polymer film encompasses three distinguishable layers along the x-axis: A center layer containing increasing amounts of EVOH and two layers left and right containing little to no EVOH, which agrees with the expected composition of the polymer film based on the manufacturing process. The false-color image composed from the integration of the ν(C–C) stretching mode, however, suggests the presence of significant amounts of PP in the middle EVOH layer, which seems rather unlikely. For area 2 analogous false color images area shown (Fig. 3, top right), revealing a similar structure albeit with a non-centered EVOH layer with increased absorption at the ν(C–O) band. On the other hand, neither the 1168 cm^{-1} nor the 973 cm^{-1} absorption band (results not shown) revealed meaningful concentration distribution maps for PP indicating that the selectivity of these bands for PP is not sufficient in the current analysis to reveal its concentration distribution within the sample. This lack of selectivity can be attributed mainly to physical effects, such as scattering and/or interference effects. Therefore, the next step was to carry out multivariate analysis of the hyperspectral data cube in order to enhance the selectivity for the two polymers present in the MLPF sample.

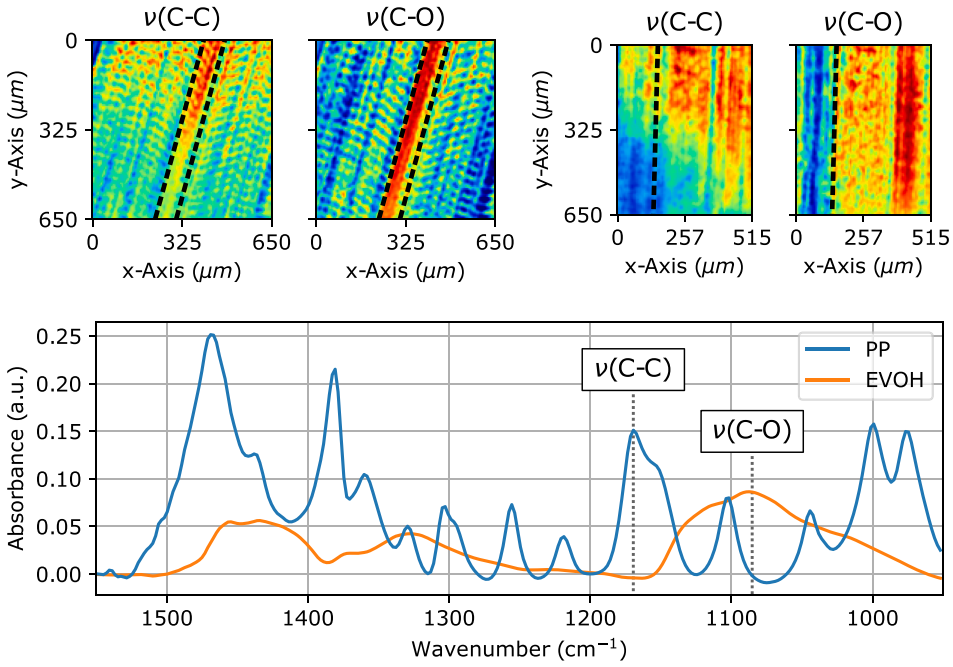

Fig. 3. Analysis of selective bands. Top panel: distribution of backbone v(C–C) (1168 cm^{-1}) and v(C–O) stretching (1080 cm^{-1}) bands corresponding to area 1 (left two plots) and area 2 (right two plots). Red and blue regions indicate high and low intensity of the corresponding absorption band, respectively. Black dashed lines indicate the borders between EVOH-rich and PP-rich areas as determined by MCR (see Fig. 5). Bottom: Reference spectra of polypropylene (PP) in blue and ethylene-vinyl alcohol co-polymer (EVOH) in orange, recorded with a conventional FTIR microscope in reflection geometry. (For interpretation of the references to color in this figure legend, the reader is referred to the Web version of this article.)

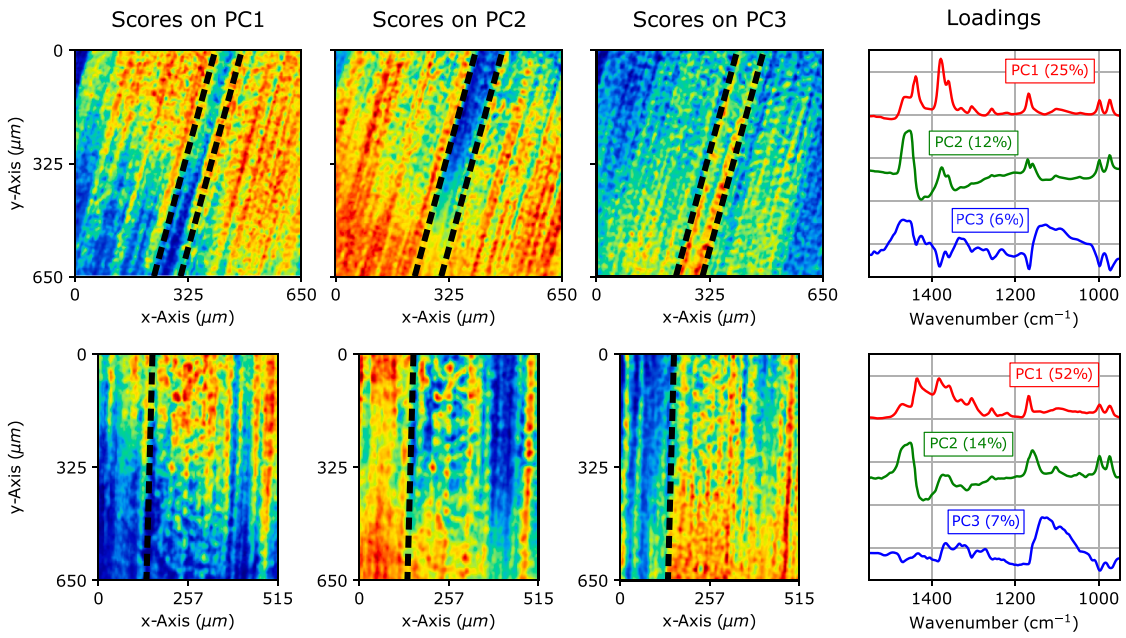

Fig. 4. Principal component analysis of area 1 (top) and area 2 (bottom). The left three graphs show the scores on the first three principal components (from left to right) represented as a false color image with blue indicating lowest and red indicating highest scores. Black dashed lines indicate the borders between EVOH-rich and PP-rich areas as determined by MCR (see Fig. 5). Corresponding loadings on the first three PCs are shown in the graph on the rightmost side. The percentage of explained variance for each PC is indicated in the graphs. Note that the loadings are plotted with an offset for better visibility. (For interpretation of the references to color in this figure legend, the reader is referred to the Web version of this article.)

3.1. Principal component analysis (PCA)

Fig. 4 shows false-color images for the two investigated areas, where the color channel encodes the score of the corresponding pixel's spectrum on the first three principal components (PCs) from blue (lowest) to red (highest). These three PCs together account for 41% and 73% of the variation in the data for area 1 and area 2, respectively. Vertically shifted loadings on the first three PCs for the two areas are shown in the plots on the very right side in Fig. 4 (PC1, PC2 and PC3 from top to bottom) with the explained variance for each PC indicated in the graph above the respective loadings.

Comparing the loadings patterns with the reference spectra from Fig. 3, the first (red) and third (blue) PC largely cover the spectral features of PP and EVOH, respectively. The contributions of these PCs in the false-color image for area 1 indicates higher EVOH concentration in the middle layer sandwiched by a mixture layer containing PP and EVOH with rising concentration of PP with increasing distance from the middle layer. This is in good agreement with the manufacturing process. The second PC (green) also has some of the features that can be attributed to PP (e.g. peaks at 973 cm^{-1} and 1000 cm^{-1}) and the scores on PC2 depict a similar spatial distribution to PC1 with higher values towards the edges of the sample. However, it additionally shows a feature with strong positive contribution around 1460 cm^{-1} followed by a largely negative contribution at 1420 cm^{-1}. Since this feature does not resemble any of the expected spectral features of the two constituents of the MLPF, it is assumed that its origin is mainly physical in nature (e.g. sample tilting or surface roughness). Generally, the scores on all PCs in area 1 show a gradual increase (PC1) or decrease (PC2 and PC3) from the bottom left to the top right of the image. This strongly suggests a slight tilting of the sample along this direction influencing all PCs and their respective loadings, demonstrating PCAs lack of ability to separate chemical and physical influences in infrared absorption spectra. The same tilting effect is also evident in the false-color image of the backbone ν(C–C) stretching band in Fig. 3.

Similarly, the PCA analysis of area 2 hints towards a PP-rich layer at the left of the image and an EVOH-rich layer towards the right, although for area 2 this assumption is mainly supported by the scores on PC2 and PC3. The scores on PC1, however, mainly depict a rise from the bottom to the top of the image, probably stemming from slight tilting of the measured sample, as also visible in the false-color image of the backbone ν(C–C) stretching band in area 2 (Fig. 3).

Notably, the PC1 and PC2 loadings of both areas are very similar, whereas PC3 displays different features in the region between 1400 cm^{-1} and 1500 cm^{-1} indicating presence of different sources of variation underlying area 1 and 2. Since the loadings in PCA only give an indirect picture of the signals of the underlying molecular species, we next undertook a multivariate curve resolution (MCR) analysis in order to better extract the putative IR absorption spectra of the individual constituents from the HSI data.

3.2. Multivariate curve resolution (MCR)

The previously performed exploratory analysis using PCA already allowed to visualize the similarity between the spectral contributions for the two analyzed areas. From these results, a four-component MCR decomposition of the multiset data was considered because more reliable results and better data fit could be obtained. The results obtained with MCR-ALS analysis are provided in Fig. 5. They correspond to a LOF of 28%, and an r^2 of 92% which are found satisfactory when compared to the amount of variance described by the PCA models. By construction of the multiset structure, the first two components are constrained to have the same spectra, whereas the third (resp. fourth) component is constrained to be absent in area 2 (resp. area 1) in order to describe spectral variations that are specific to each of the two areas. This four-component multiset setting is in good agreement with the PCA investigation discussed above and also results from the three-component MCR-ALS analysis of individual data sets, which revealed the existence of slight differences between the spectral composition of the two images (results not shown). These spectral differences could not be fully corrected by preprocessing and might originate from the fact that the samples are positioned differently or due to different surface topologies. The left side of Fig. 5 shows false-color images depicting the concentration distribution maps obtained by MCR-ALS analysis, whereas the corresponding spectra are shown on the right.

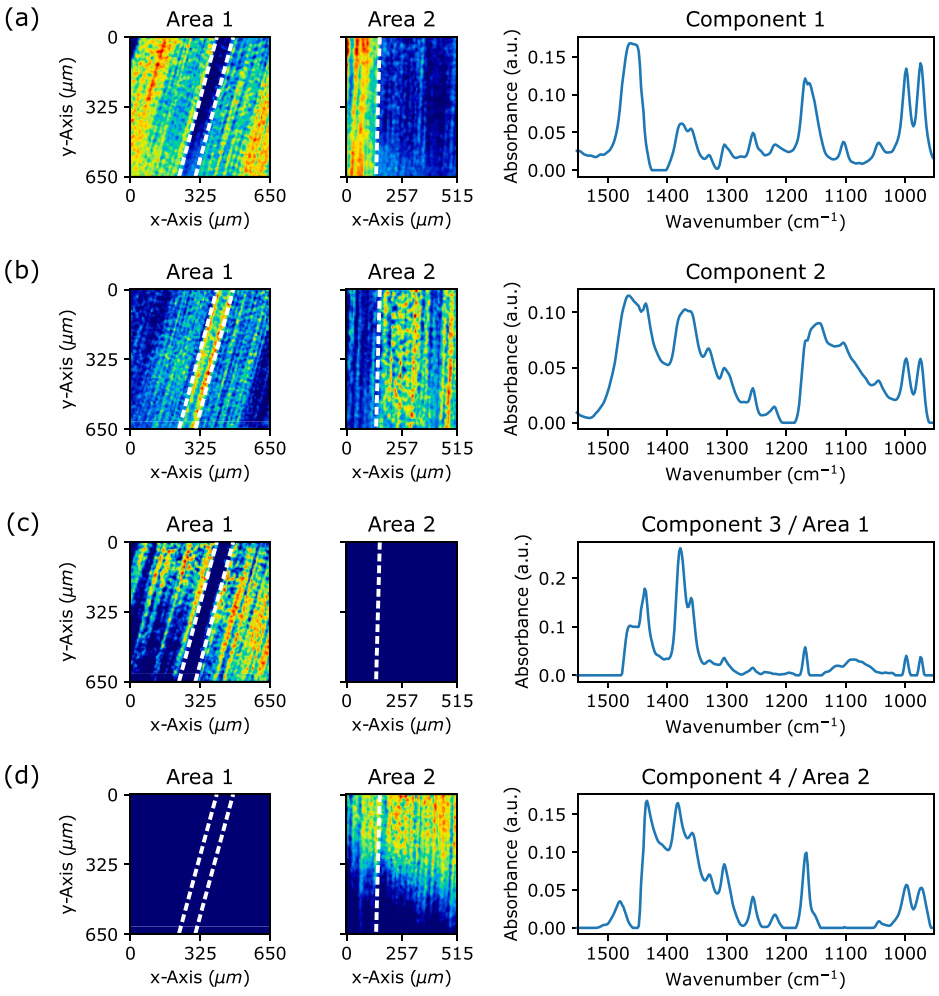

Fig. 5. (a)–(d) Multivariate curve resolution of the MLPF sample. On the left, false-color images indicating the concentration distribution maps for the two investigated areas for the respective component plotted on the right side. White dashed lines are added as a guide to the eye to distinguish between EVOH-rich (strong contribution of component 2) and PP-rich (strong contribution of component 1) areas in the image. (For interpretation of the references to color in this figure legend, the reader is referred to the Web version of this article.)

The concentration distribution maps of the first two components draw a very reasonable picture of both sample areas, assuming components 1 and 2 represent PP and EVOH, respectively. The obtained distribution recreates some of the features that are visible in the false color images of the first three principal components shown in Fig. 4 but generally manages to much better distinguish between the chemically different areas in the obtained hyperspectral image.

The spectrum corresponding to the first MCR component (Fig. 5 (a), right) is characterized by strong absorption from the δ(C–H) deformation band around 1460 cm^{-1}, ν(C–C) backbone stretching band at 1168 cm^{-1} as well as highly pronounced contributions from the bands at 998 cm^{-1} and 973 cm^{-1}, all of which are characteristic for PP. This clearly backs up the assumption that component 1 corresponds to PP that can already be drawn from the spatial distribution image. Compared to the univariate analysis at the ν(C–C) band shown in Fig. 3, which is supposedly selective for PP, the obtained distribution looks very different and much closer fits the expectation.

The spatial distribution of component 2 closely resembles the distribution obtained via univariate analysis at the position of the ν(C–O) band, which is supposedly selective for EVOH. However, in addition to strong contributions in the spectral range between 1000 cm^{-1} and 1150 cm^{-1} which coincides with the broad absorption of pure EVOH (evident from the reference spectrum in Fig. 2), the second MCR component (Fig. 5 (b), right) also exhibits pronounced absorption features specific for PP indicating incomplete unmixing of PP and EVOH by MCR.

As explained above, the information in Fig. 5 (c) corresponds to an additional spectral component (component 3) that is only present in area 1. Considering both the concentration distribution observed in area 1 and the corresponding spectral profile, this information can be attributed mostly to PP. Two putative PP species were thus required to properly describe the data for area 1 (encoded in components 1 and 3). The first (component 1) clearly shows all the characteristic PP bands, while the second (component 3) shows significant contributions from EVOH (seen in the broad peak around 1100 cm^{-1}). Interestingly, despite this EVOH-contribution, the spatial distribution of component 3 as seen on the left in Fig. 5 (c), shows no contribution of this component in the center layer, which is expected to contain mostly EVOH (see also Fig. 4), but is present in the surrounding mixing layers.

As discussed above, MCR analysis manages to provide a meaningful description of the available data. However, all the measured spectral variation is described in an undifferentiated way, which might translate into additional components in systems for which different spectral signatures are observed for one chemical species, due to physical effects, instrumental artifacts or deviation from ideal bilinearity. In the situation investigated here, the joint analysis of two different areas of the same sample has revealed that a "naïve" two-component (PP and EVOH) decomposition is not justified (observed). The spectral complexity is actually higher, as revealed by the PCA investigation of the individual sample areas. The most reliable description obtained requires four components, the two major ones being shared by the two individual areas and the remaining accommodating deviations from the ideal situations, as described above. As a result, the spectral interpretation of these components is not as straightforward as it may have been expected, because some level of spectral mixing is still unavoidably observed. However, the corresponding images (concentration distribution maps) can provide additional insight into the nature of the

corresponding component. In the case of component 4, where the spatial distribution shows an unexpected concentration gradient along one dimension of the sample where no difference in chemical composition is expected, one can assume that not chemical, but mainly physical information is described. The shape of the corresponding spectral profile, that can hardly be attributed to any of the expected constituents, would tend to further strengthen this assumption.

4. Conclusion

In the present contribution, we have employed QCL-based mid-infrared hyperspectral imaging to the analysis of a polypropylene/ethylene-vinyl-alcohol polymer film. Due to their high spatial resolution, QCL-based imaging systems are particularly well suited to characterize chemically heterogeneous systems such as the investigated MLPF sample. However, as outlined above, alignment, sample preparation (planarity) and physical effects such as e.g. scattering or interference can significantly hamper the analysis of hyperspectral imaging data and might require extensive data treatment to draw the right conclusions. In particular, results from univariate analysis of putative bands that are supposed to be selective for a particular chemical constituent can draw a misleading picture of the sample at hand and thus should always be taken with a grain of salt. On the other hand, multivariate methods can draw a holistic picture of the sample and help resolving the concentration distribution of individual chemical constituents. Visualization of the scores on the dominant PCs, explaining most of the variation in the data, by means of false-color images and analysis of the corresponding loadings vectors is a good starting point when trying to understand the chemistry of the sample at large. Subsequent iterations of applying advanced (i.e. multiset) MCR-ALS analyses using different ranks and/or constraints on raw and preprocessed data in combination with expert/process knowledge can subsequently shed further light on the subtleties related to the chemistry of the sample and the physical phenomena that interfere with the data acquisition process.

Data availability

The raw/processed data required to reproduce these findings cannot be shared at this time as the data also forms part of an ongoing study.

Authorship contributions

Category 1:
Conception and design of study:
R. Zimmerleiter, M. Brandstetter, J. Kilgus
Acquisition of data:
R. Zimmerleiter, M. Godejohann, J. Kilgus, M. Brandstetter
Analysis and/or interpretation of data:
R. Zimmerleiter, R. Nikzad-Langerodi, C. Ruckebusch, K. Duswald, J. Kilgus
Category 2:
Drafting of the Manuscript:
R. Zimmerleiter, R. Nikzad-Langerodi, C. Ruckebusch, J. Kilgus
Revising the manuscript critically for important intellectual content:
M. Brandstetter, M. Godejohann, K. Duswald
Category 3:
Approval of the version of the manuscript to be published:
R. Zimmerleiter, R. Nikzad-Langerodi, C. Ruckebusch, M. Godejohann, J. Kilgus, K. Duswald, M. Brandstetter

Declaration of competing interest

The authors declare that they have no known competing financial interests or personal relationships that could have appeared to influence the work reported in this paper.

Acknowledgements

The authors are thankful for lending of the Spero®QT by Daylight Solutions (USA) via MG Optical Solutions (Germany).

Financial support was provided by the Austrian research funding association (FFG) under the scope of the COMET programme within the research project Photonic Sensing for Smarter Processes (PSSP) (contract #871974). This programme is promoted by BMK, BMDW, the federal state of Upper Austria and the federal state of Styria, represented by SFG. Further financial support was supplied by the strategic economic- and research program "Innovative Upper Austria 2020″ of the province of Upper Austria and the project "multimodal and in-situ characterization of inhomogeneous materials" (MiCi) by the federal government of Upper Austria and the European Regional Development Fund (EFRE) in the framework of the EU-program IWB2020.

The second author acknowledges support by the Federal Ministry for Climate Action, Environment, Energy, Mobility, Innovation and Technology (BMK), the Federal Ministry for Digital and Economic Affairs (BMDW), and the Province of Upper Austria in the frame of the COMET - Competence Centers for Excellent Technologies programme managed by Austrian Research Promotion Agency FFG and the COMET Center CHASE.

References

[1] A.A. Gowen, C.P. O'Donnell, P.J. Cullen, G. Downey, J.M. Frias, Hyperspectral imaging - an emerging process analytical tool for food quality and safety control, Trends Food Sci. Technol. 18 (2007) 590–598, https://doi.org/10.1016/j.tifs.2007.06.001.

[2] D.J. Mulla, Twenty five years of remote sensing in precision agriculture: key advances and remaining knowledge gaps, Biosyst. Eng. 114 (2013) 358–371, https://doi.org/10.1016/j.biosystemseng.2012.08.009.

[3] G.J. Edelman, E. Gaston, T.G. van Leeuwen, P.J. Cullen, M.C.G. Aalders, Hyperspectral imaging for non-contact analysis of forensic traces, Forensic Sci. Int. 223 (2012) 28–39, https://doi.org/10.1016/j.forsciint.2012.09.012.

[4] P. Gattinger, J. Kilgus, I. Zorin, G. Langer, R. Nikzad-Langerodi, C. Rankl, M. Gröschl, M. Brandstetter, Broadband near-infrared hyperspectral single pixel imaging for chemical characterization, Opt Express 27 (2019) 12666, https://doi.org/10.1364/OE.27.012666.

[5] P.W.T. Yuen, M. Richardson, An introduction to hyperspectral imaging and its application for security, surveillance and target acquisition, Imag. Sci. J. 58 (2010) 241–253, https://doi.org/10.1179/174313110X12771950995716.

[6] M. Diem, A. Mazur, K. Lenau, J. Schubert, B. Bird, M. Miljković, C. Krafft, J. Popp, Molecular pathology via IR and Raman spectral imaging, J. Biophot. 6 (2013) 855–886, https://doi.org/10.1002/jbio.201300131.

[7] C. Krafft, D. Codrich, G. Pelizzo, V. Sergo, Raman and FTIR microscopic imaging of colon tissue: a comparative study, J. Biophot. 1 (2008) 154–169, https://doi.org/10.1002/jbio.200710005.

[8] C. Gasser, J. Kilgus, M. Harasek, B. Lendl, M. Brandstetter, Enhanced mid-infrared multi-bounce ATR spectroscopy for online detection of hydrogen peroxide using a supercontinuum laser, Opt Express 26 (2018) 12169, https://doi.org/10.1364/oe.26.012169.

[9] I. Zorin, J. Kilgus, K. Duswald, B. Lendl, B. Heise, M. Brandstetter, Sensitivity-enhanced fourier transform mid-infrared spectroscopy using a supercontinuum laser source, Appl. Spectrosc. 74 (2020) 485–493, https://doi.org/10.1177/0003702819893364.

[10] C. Kuepper, A. Kallenbach-Thieltges, H. Juette, A. Tannapfel, F. Großerueschkamp, K. Gerwert, Quantum cascade laser-based infrared microscopy for label-free and automated cancer classification in tissue sections, Sci. Rep. 8 (2018) 1–10, https://doi.org/10.1038/s41598-018-26098-w.

[11] A. Kallenbach-Thieltges, F. Großerueschkamp, H. Jütte, C. Kuepper, A. Reinacher-Schick, A. Tannapfel, K. Gerwert, Label-free, automated classification of microsatellite status in colorectal cancer by infrared imaging, Sci. Rep. 10 (2020) 1–13, https://doi.org/10.1038/s41598-020-67052-z.

[12] A. Ebner, R. Zimmerleiter, C. Cobet, K. Hingerl, M. Brandstetter, J. Kilgus, Sub-second quantum cascade laser based infrared spectroscopic ellipsometry, Opt. Lett. 44 (2019) 3426, https://doi.org/10.1364/ol.44.003426.

[13] J. Kilgus, G. Langer, K. Duswald, R. Zimmerleiter, I. Zorin, T. Berer, M. Brandstetter, Diffraction limited mid-infrared reflectance microspectroscopy with a supercontinuum laser, Opt Express 26 (2018) 30644, https://doi.org/10.1364/OE.26.030644.

[14] P. Bassan, M.J. Weida, J. Rowlette, P. Gardner, Large scale infrared imaging of tissue micro arrays (TMAs) using a tunable Quantum Cascade Laser (QCL) based microscope, Analyst 139 (2014) 3856–3859, https://doi.org/10.1039/c4an00638k.

[15] A. Barroso Pena, S. Ketelhut, M. Godejohann, B. Kemper, J. Schnekenburger, Optical imaging methods for label free detection of microplastics in cells, tissues and environmental organisms (Conference Presentation), in: D.L. Farkas, J.

F. Leary, A. Tarnok (Eds.), Imaging, Manip. Anal. Biomol. Cells, Tissues XVIII, SPIE, 2020, p. 43, https://doi.org/10.1117/12.2546098.
[16] J. Lange, Y. Wyser, Recent innovations in barrier Technologies for plastic packaging - a review, Packag. Technol. Sci. 16 (2003) 149–158, https://doi.org/10.1002/pts.621.
[17] K.K. Mokwena, J. Tang, Ethylene vinyl alcohol: a review of barrier properties for packaging shelf stable foods, Crit. Rev. Food Sci. Nutr. 52 (2012) 640–650, https://doi.org/10.1080/10408398.2010.504903.
[18] P.H.C. Eilers, H.F.M. Boelens, Baseline correction with asymmetric least squares smoothing, Leiden Univ. Med. Cent. Rep. 5 (2005) 1–26, https://doi.org/10.1021/ac034173t.
[19] H. Hotelling, Analysis of a complex of statistical variables into principal components, J. Educ. Psychol. 24 (1933) 417–441, https://doi.org/10.1037/h0071325.
[20] M. Meloun, J. Čapek, P. Mikšík, R.G. Brereton, Critical comparison of methods predicting the number of components in spectroscopic data, Anal. Chim. Acta 423 (2000) 51–68, https://doi.org/10.1016/S0003-2670(00)01100-4.
[21] C. Ruckebusch, L. Blanchet, Multivariate curve resolution: a review of advanced and tailored applications and challenges, Anal. Chim. Acta 765 (2013) 28–36, https://doi.org/10.1016/j.aca.2012.12.028.
[22] R. Tauler, Multivariate curve resolution applied to second order data, Chemometr. Intell. Lab. Syst. 30 (1995) 133–146, https://doi.org/10.1016/0169-7439(95)00047-X.
[23] S. Hugelier, O. Devos, C. Ruckebusch, On the implementation of spatial constraints in multivariate curve resolution alternating least squares for hyperspectral image analysis, J. Chemom. 29 (2015) 557–561, https://doi.org/10.1002/cem.2742.
[24] W.H. Lawton, E.A. Sylvestre, Self modeling curve resolution, Technometrics 13 (1971) 617–633, https://doi.org/10.1080/00401706.1971.10488823.
[25] A. de Juan, S. Rutan, M. Maeder, R. Tauler, Multivariate curve resolution chapters, Compr. Chemom. 2 (2009) 207–558.
[26] M. Ghaffari, N. Omidikia, C. Ruckebusch, Essential spectral pixels for multivariate curve resolution of chemical images, Anal. Chem. 91 (2019) 10943–10948, https://doi.org/10.1021/acs.analchem.9b02890.
[27] W. Xu, S. Asai, M. Sumita, Spectroscopic study of ethylene vinyl alcohol copolymer and poly (vinyl alcohol), J. Fiber Sci. Technol. 53 (1997) 174–182, https://doi.org/10.2115/fiber.53.5_174.
[28] J. Karger-Kocsis, Polypropylene : an A-Z Reference, Springer Netherlands, Dordrecht, 1999, https://doi.org/10.1007/978-94-011-4421-6.
[29] D.R. Burfield, P.S.T. Loi, The use of infrared spectroscopy for determination of polypropylene stereoregularity, J. Appl. Polym. Sci. 36 (1988) 279–293, https://doi.org/10.1002/app.1988.070360203.